ChemCatChem

Research Article
doi.org/10.1002/cctc.202500659

Chemistry Europe
European Chemical Societies Publishing

www.chemcatchem.org

Rationalizing Catalytic Performances of Mo/W-(Oxy)Carbides for Hydrodeoxygenation Reaction

Raghavendra Meena,[a, b] Koen Marcus Draijer,[a] Bastiaan van Dam,[a] Han Zuilhof,[b, c] Johannes Hendrik Bitter,[a] and Guanna Li*[a]

Hydrodeoxygenation (HDO) reactions are among the most important reactions for the valorization of biomass to value-added chemicals. Transition metal carbides (TMCs) are promising alternative HDO catalysts to platinum group metals. However, it is known that these TMCs have the tendency to partially oxidize themselves in the presence of oxygen or oxygen-containing compounds, which makes it a challenge to identify the nature of the true active site under relevant reaction conditions. In this paper, first, we analyze the surface structure of transition metal oxycarbides (TMOCs), that is, Mo_2CO_x and W_2CO_x. Further, taking the HDO of *n*-butyric acid to *n*-butane with hydrogen as an example, we rationalize the differences in HDO performances of TMOCs as compared to TMCs (Mo_2C and W_2C) using density functional theory, ab initio molecular dynamics, and microkinetic modelling. It is found that the O* domains on the surface of TMOCs enhance the HDO activity by easing the dissociation of the C-O bond and promoting the hydrogenation reactions, as compared to pure TMCs. Furthermore, microkinetic modelling analysis shows that Mo_2CO_x is a more active and selective catalyst for alkane production compared to Mo_2C, W_2C, and W_2CO_x. These insights could guide the manipulation of efficient carbide-based HDO catalysts for biomass conversion.

1. Introduction

To mitigate the negative impact of the use of fossil resources on our climate renewable feedstocks, sustainable conversions are needed to make chemicals, materials and fuels. Biomass is such a renewable feedstock. However, the oxygen content in biomass is typically too high for current applications; therefore, deoxygenations are needed. As a case in point the catalytic deoxygenation of lipids present in biomass is required to obtain chemicals such as alkenes, alkanes, and alcohols.[1,2] Thus, hydrodeoxygenation (HDO) of long-chain fatty acids (LCFAs) has attracted much attention for the conversion of biomass to value-added chemicals.[3,4] Platinum group metals (PGMs) such as platinum (Pt) and palladium (Pd) have been shown to be viable catalysts for HDO.[5] While these catalysts show good reaction activity, limited availability and associated high costs make them unattractive for industrial use. Therefore, efforts are needed to find highly efficient, cheap and sustainable alternatives to PGMs for HDO reactions.

Transition metal carbides (TMCs) have been shown to be viable alternatives to PGMs for HDO reactions.[6] Especially, tungsten carbide (W_2C) and molybdenum carbide (Mo_2C) have received much attention[7–11] since Levy and Boudart[12] demonstrated that these materials exhibit catalytic properties like noble metal-based catalysts. These authors attribute the PGM-like properties of TMCs to the carbon incorporation in the metal lattice, leading to a higher d-band electronic density of states, closer to the Fermi level. Decades later, Iglesia et al.[13] showed that WC and W_2C catalyzed hydrogenolysis, hydrogenation, and dehydrogenation reactions with high selectivity, which were previously only documented for Pt, Ir, and Au metals. Choi et al. further demonstrated that increased carburization (carbon content) of the transition metal increased its PGM-like catalytic properties.[14] More recently, many research groups have studied structure-activity relationships of TMCs for hydrogenation, dehydrogenation, HDO, and many other reactions, and successfully demonstrated TMCs' ability to catalyze a wide range of reactions.[8,10,11,15,16] Prats et al. have summarized most of these findings and other recent progress in utilizing TMCs as supports for catalytic metal particles.[17] The interesting behavior and versatility of reactions TMCs could catalyze has incentivized research into their intrinsic structure-activity relationships.

However, a potential downside of using these TMCs as catalysts is the ease at which they (partially) oxidize in the presence of oxygen or oxygen-containing compounds, thereby resulting in the formation of transition metal oxycarbides (TMOCs), that is, Mo_2CO_x and W_2CO_x. Although not much research on the nature of W_2CO_x is available at this moment, the activity and nature of molybdenum oxycarbide (Mo_2CO_x) have been explored.[18] Chen et al. studied the effects of oxygen content on rates and

[a] R. Meena, K. M. Draijer, B. van Dam, Prof. J. H. Bitter, Dr. G. Li
Biobased Chemistry and Technology, Wageningen University & Research, Bornse Weilanden 9, Wageningen 6708WG, The Netherlands
E-mail: guanna.li@wur.nl

[b] R. Meena, Prof. H. Zuilhof
Laboratory of Organic Chemistry, Wageningen University & Research, Stippeneng 4, Wageningen 6708WE, The Netherlands

[c] Prof. H. Zuilhof
China-Australia Institute for Advanced Materials and Manufacturing, Jiaxing University, Jiaxing 314001, China

selectivity of *m*-Cresol HDO for toluene synthesis.[19] These authors showed that exposure to molecular oxygen resulted in oxygen (0.23 O/Mo_{bulk}) being deposited on Mo_2C at low oxidant pressure (1 kPa) and temperature (333 K), and that the toluene synthesis rate was reduced 10-fold due to poisoning of the active surface metal-like sites by adsorbed oxygen. Also, Kumar et al. reported that oxygen deposition (0.3 O/Mo_{bulk}) from the reactant oxygenate was observed during the HDO of acetic acid.[20] Density functional theory (DFT) and microkinetic reactor modelling study by Ammal et al. showed that oxyphilic Mo_2C (100) surface is active for HDO of glycerol to hydroxypropanal.[21] These authors, in their model, assume that Mo_2C surface is fully oxygenated with acid-base (OH, O) pairs, that is, 0.5 monolayer of oxygen (ML_O). The -OH groups promote H_2O formation, resulting in oxygen vacancies and exposed active Mo sites which promote the C-O cleavage. Kurlov et al. demonstrated that the dry reforming of methane was promoted over oxygen-modified 2D-Mo_2C, compared to Mo_2C, where they assume that the surface of Mo_2C is occupied with oxygen (0.67 ML_O).[22]

Based on the aforementioned studies, it is expected that catalytic HDO of free fatty acids on TMCs (Mo_2C, W_2C) would result in high levels of oxygen being deposited on the catalyst surface, essentially forming TMOCs (Mo_2CO_x, W_2CO_x). Therefore, to model such a surface, we take inspiration from experiments by Ovári et al.[23] where they demonstrated the complete removal of surface carbon (as CO) from Mo_2C (100) upon interaction with O_2 at 500–600 K using mass spectrometry. The C-vacancies are then filled with oxygen atoms. Later, Shi et al.[24] also provided mechanisms for this surface carbon removal as CO and chemisorption of oxygen over Mo_2C (011, 101) surfaces. More recently, Sun et al. show that deposition of a layer of oxygen on the Mo_2C surface to form Mo_2CO_x species increases the stability of the catalyst and promotes C-O bond scission (compared to Mo_2C) for CO_2 hydrogenation reaction.[25] Hence, in our study, we utilize a similar model where the carbon atoms in the top layer of the widely studied Mo_2C and W_2C catalysts[26–28] are substituted with oxygen to represent the TMOCs surface, corresponding to 0.5 ML_O, as depicted in Figure 1A. The stability of such surfaces (oxygen-modified Mo_2C) is supported by the work of Likith et al.[29] and Li et al as well.[30] These authors evaluated the thermodynamic stabilities of different compositions of molybdenum oxycarbides formed from Mo_2C in the reduction condition of H_2 evolution reaction and the results were validated by experiments. They show that Mo_2CO_x is stable under reduction conditions with a C:O ratio of 2:1, which is consistent with the model employed in this study.

It is important to understand how the presence of oxygen on the surface alters the activity and selectivity of TMOCs compared to pure TMCs for HDO of biobased feedstock. In this work, we rationalized the catalytic HDO performances of TMCs (Mo_2C, W_2C), and TMOCs (Mo_2CO_x, W_2CO_x) by a comprehensive reaction mechanism study of the HDO reaction of *n*-butyric acid to *n*-butane. DFT reaction energies in combination with MKM were used in identifying the critical intermediates, rate-determining elementary reaction step(s), and the activity and selectivity differences of the catalysts studied. Based on these analyses, it is found that C—OH bond dissociation is one of the most critical steps and TMOCs are more active and selective toward alkanes compared to TMCs.

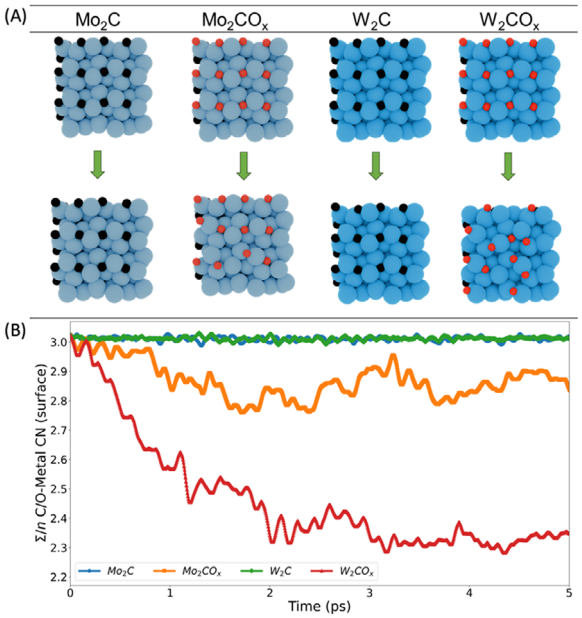

Figure 1. (A) Evolution of the catalytic surfaces at a reaction temperature of 623 K, simulated for 5 ps using AIMD. (B) The average coordination number (CN) of C/O-Metal (Mo/W) per surface C/O over time. NOTE: ***n*** is the number of C or O atoms on the surface, that is, 12.

2. Results and Discussion

2.1. Carbide and Oxycarbide Model Rationalization

Butyric acid was chosen in this study as a model compound for fatty acids, as it possesses a carboxyl acid moiety and an aliphatic tail, which are also present in fatty acids. For the TMC surface models, we chose the stable Mo_2C (101) and W_2C (101) terminations, while for TMOCs we took inspiration from previous experimental[19,20,22,23] and theoretical studies,[24,29,30] and built models in which the top-layer C atoms in Mo_2C (101) and W_2C (101) were replaced by O atoms, as shown in Figure 1A.

From the initial static DFT geometry relaxations, no significant surface reconstruction was observed for both the carbide and oxycarbide surfaces. To further evaluate the surface structure, we performed AIMD simulations of the four catalysts under study to better understand the nature of active sites (metal center) under reaction conditions. We start the simulations using static DFT optimized geometries. Figure 1A shows the initial geometries (top) of the clean catalytic surfaces, and final geometries (bottom) after 5 ps of AIMD simulation at 623 K. Further, we quantified (Figure 1B) the change in coordination environment of the active surface metal site by calculating the average C-Metal (Mo or W) coordination number (CN) per surface C in TMCs, and O-Metal CN per surface O in TMOCs. The results reveal that TMC surfaces are stable with negligible surface reconstruction, while TMOC surfaces are much more dynamic, as the surface continuously undergoes reconstruction, that is, the average CN

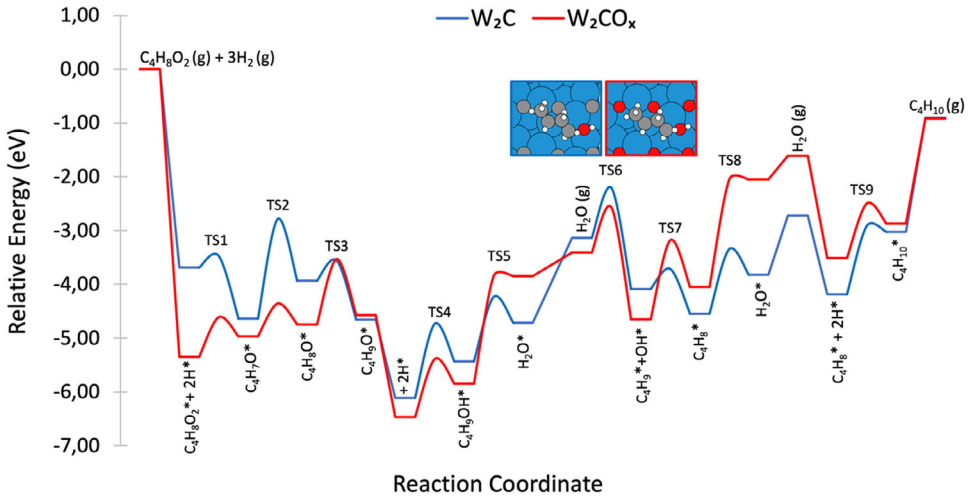

Figure 2. The reaction energy diagram for the HDO reaction of *n*-butyric acid over W_2C and W_2CO_x catalysts.

of O-Metal on the surface changes from 3.00 to ~2.85 in the case of Mo_2CO_x, and changes from 3.00 to ~2.40 in the case of W_2CO_x. We speculate that a reduction in these CNs leads to a more active metal center. While the CN changes, these surface O atoms stay on the surface and no diffusion into the sublayer was observed.

2.2. HDO Reaction Mechanism

We studied the HDO reaction mechanism of butyric acid over Mo_2C (101), W_2C (101), Mo_2CO_x (101), and W_2CO_x (101) catalysts. In all cases, we start with a clean slab, butyric acid and three molecules of molecular H_2 to produce butanal, followed by butanol, butene, and butane products. This sequential manner is based on experimental observations. For example, Stellwagen et al.[10] and Marlene et al.[16] showed in their work the stearic acid concentration and product distribution over time of Mo_2C and W_2C. Their product distribution shows that Mo_2C and W_2C follow the HDO pathway of substrate reduction to aldehyde, followed by alcohol, alkene and alkane for the removal of oxygen content from stearic acid. Further, we have shown in our previous work, [15] H- species on the surface can easily hop over the surface under reaction conditions (T = 623 K, pH_2 = 30 bar). Subsequently, the reactant is adsorbed on the surface, and then the elementary steps take place on the surface (denoted by *). Eventually, the final product, that is, butane and two molecules of water (H_2O) are desorbed from the surface. Throughout the text, the carbon atom of the acidic group is referred to as C1. The overall reaction is as following.

$$C_4H_8O_2 + 3H_2 \rightarrow C_4H_{10} + 2H_2O.$$

2.3. HDO over W_2C and W_2CO_x

The reaction energy profiles for the HDO reaction over W_2C and W_2CO_x surfaces are shown in Figure 2. First, the butyric acid and dissociative H_2 adsorption (in a homolytic manner) over W-W metal active sites is an exothermic process over W_2C ($\Delta E = -3.69$ eV) and W_2CO_x ($\Delta E = -5.35$ eV). Butyric acid ($C_4H_8O_2$*) then undergoes C—OH activation via TS1 and forms C_4H_7O* and OH* exothermically over W_2C ($E_a = 0.22$ eV, $\Delta E = -0.99$ eV), and endothermically over W_2CO_x ($E_a = 0.74$ eV, $\Delta E = 0.38$ eV). Here, we also consider a pathway where hydrogenation of the carbonyl group happens first instead of C—OH activation over all four catalysts under study. It was found that the resulting intermediate ($C_3H_7C(OH)_2$*) from hydrogenation reaction is at least 0.80 eV less stable than the intermediate (C_4H_7O*+ OH*) upon C—OH cleavage. The difference in the C—OH activation barrier in TS1 is due to the strong adsorption of butyric acid over W_2CO_x. The butyric acid is adsorbed over W_2CO_x via bidentate W-O bonds (oxygen from butyric acid), compared to monodentate W-O bond in W_2C. The terminal C atom (C1) in C_4H_7O* is then hydrogenated via TS2 to produce butanal (C_4H_8O*) in the case of W_2C ($E_a = 1.84$ eV, $\Delta E = 0.70$ eV); this step is kinetically challenging as C1 is strongly adsorbed on W atom and resists hydrogenation. This hydrogenation step is much easier in the case of W_2CO_x ($E_a = 0.61$ eV, $\Delta E = 0.22$ eV) due to the weak physisorption of C1 on W-atom. Subsequently, the C1 atom in C_4H_8O* is hydrogenated again via TS3 to produce C_4H_9O*, a precursor for butanol (C_4H_9OH*) formation. The O atom in C_4H_9O* is then hydrogenated via TS4 to produce C_4H_9OH* over W_2C ($E_a = 1.38$ eV, $\Delta E = 0.69$ eV), which is similar to W_2CO_x ($E_a = 1.08$ eV, $\Delta E = 0.62$ eV). C_4H_9OH* then undergoes C—OH activation via TS6 (local structures in Figure 2) to produce C_4H_9* and OH* over W_2C ($E_a = 0.93$ eV, $\Delta E = -0.94$ eV), which is also similar but slightly easier in W_2CO_x ($E_a = 0.84$ eV, $\Delta E = -1.24$ eV), implying a better activity of W_2CO_x for deoxygenation. The C1 atom in C_4H_9* then undergoes deprotonation via TS7 to produce butene (C_4H_8*). This process is much easier over W_2C ($E_a = 0.37$ eV, $\Delta E = -0.46$ eV) than over W_2CO_x ($E_a = 1{,}47$ eV, $\Delta E = -0.60$ eV). However, instead of undergoing deprotonation to C_4H_8*, C_4H_9* can readily hydrogenate to form C_4H_{10}* via TS9. This is much easier over W_2CO_x* ($E_a = 1.01$ eV, $\Delta E = 0.64$ eV) compared to dehydrogenation to C_4H_8*. The barriers TS7 and

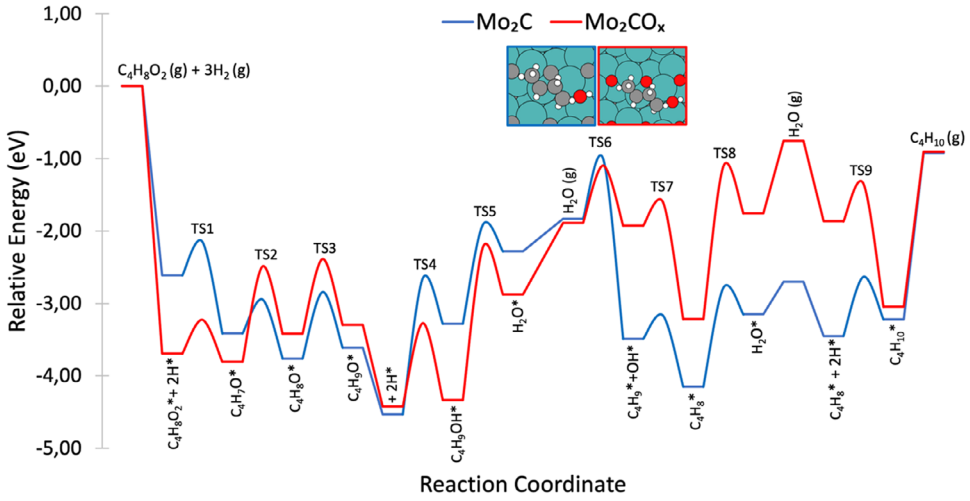

Figure 3. The reaction energy diagram for the HDO reaction of *n*-butyric acid over Mo_2C and Mo_2CO_x catalysts.

TS9 imply that these two steps compete during the reaction. The final product, C_4H_{10}*, can then be desorbed requiring a desorption energy of 2.12 eV over W_2C and 1.95 eV over W_2CO_x. Also, the OH* species on the surface can be hydrogenated to produce water (H_2O*) via TS5/8. Water formation over W_2CO_x (E_a = 2.00 eV, ΔE = 2.00 eV) is kinetically and thermodynamically much more difficult compared to W_2C (E_a = 1.20 eV, ΔE = 0.62 eV), suggesting the presence of excess H* species over W_2CO_x surface.

2.4. HDO over Mo_2C and Mo_2CO_x

Figure 3 illustrates the HDO reaction energy diagram for Mo_2C and Mo_2CO_x. The reaction energies over Mo_2C studied in our previous work[15] were used to compare with the reactivity of Mo_2CO_x catalyst studied in this work. Again, butyric acid is adsorbed over Mo_2CO_x together with homolytic H_2 dissociative adsorption over Mo-Mo metal active sites (ΔE = −3.69 eV). Butyric acid, $C_4H_8O_2$*, undergoes C—OH activation via **TS1** and forms C_4H_7O* and OH* in the case of Mo_2CO_x (E_a = 0.47 eV, ΔE = −0.11 eV), while it is kinetically difficult and thermodynamically more favorable over Mo_2C (E_a = 0.45 eV, ΔE = −0.80 eV). The C1 atom in C_4H_7O* is then hydrogenated via **TS2** to produce butanal, C_4H_8O* (E_a = 1.32 eV, ΔE = 0.39 eV). This process is kinetically less demanding in Mo_2C (Ea = 0.46 eV, ΔE = −0.35 eV) because of weaker Mo-C1 interactions compared to Mo_2CO_x. Further, the C1 atom in C_4H_8O* is hydrogenated via **TS3** to produce C_4H_9O* (E_a = 1.03 eV, ΔE = 0.12 eV), which is kinetically and thermodynamically similar to that over Mo_2C (E_a = 0.92 eV, ΔE = 0.15 eV). The O atom in C_4H_9O* is then hydrogenated via **TS4** to produce butanol, C_4H_9OH* (E_a = 1.15 eV, ΔE = 0.09 eV). This process is much more difficult over Mo_2C (E_a = 1.88 eV, ΔE = 1.25 eV), as O* is strongly stabilized over the Mo-Mo center. C_4H_9OH* undergoes C—OH activation via **TS6** (local structures in Figure 3) to produce C_4H_9* and OH* (E_a = 0.79 eV, ΔE = −0.04 eV). This step is kinetically slightly difficult over Mo_2C (E_a = 0.83 eV, ΔE = −1.66 eV); however, it is thermodynamically very favorable compared to Mo_2CO_x. The C1 atom in C_4H_9* then undergoes deprotonation via **TS7** to produce butene, C_4H_8* (E_a = 0.32 eV, ΔE = −1.29 eV), which is more favorable thermodynamically compared to Mo_2C (E_a = 0.32 eV, ΔE = −0.66 eV). Like the case of W_2C and W_2CO_x, C_4H_9* can instead be hydrogenated to form C_4H_{10}* (E_a = 0.52 eV, ΔE = −1.18 eV) via **TS9**. This step is much more favorable over Mo_2CO_x than over Mo_2C (Ea = 0.82 eV, ΔE = 0.23 eV). In the case of Mo_2CO_x, the carbon chain could easily be hydrogenated to produce butane, C_4H_{10}*, but for Mo_2C, the pathway to form C_4H_8* is more favorable. The final product, C_4H_{10}*, can then be desorbed with barriers of 2.14 eV for Mo_2CO_x, and 2.30 eV for Mo_2C, individually. Compared to Mo_2CO_x (E_a = 2.11 eV, ΔE = 1.46 eV), water formation is kinetically and thermodynamically easier over Mo_2C (E_a = 1.37 eV, ΔE = 1.00 eV).

2.5. Microkinetic Modelling (MKM)

From static DFT calculations, it is indicated that hydrogenation of unsaturated hydrocarbons is much easier over W_2CO_x and Mo_2CO_x surfaces compared to W_2C and Mo_2C. Therefore, these hydrogenation steps essentially guide their selectivity toward alkane/alkene products. However, merely looking at the kinetics and thermodynamics of different elementary reaction steps involved is not enough to compare the activity of these catalysts. Hence, we performed microkinetic modelling (MKM) using the static DFT results and experimental reaction temperature (623 K) and pressure (pH_2 = 30 bar) to obtain the macroscopic properties such as surface coverages, Campbell's degree of rate control (DRC) coefficients,[31] apparent activation energies (E_{app}), and selectivity toward alkane/alkene products.

2.6. Surface Coverages

The steady-state surface coverages are shown in Figure 4. In the case of Mo_2C (Figure 4A), we see the presence of O* domains

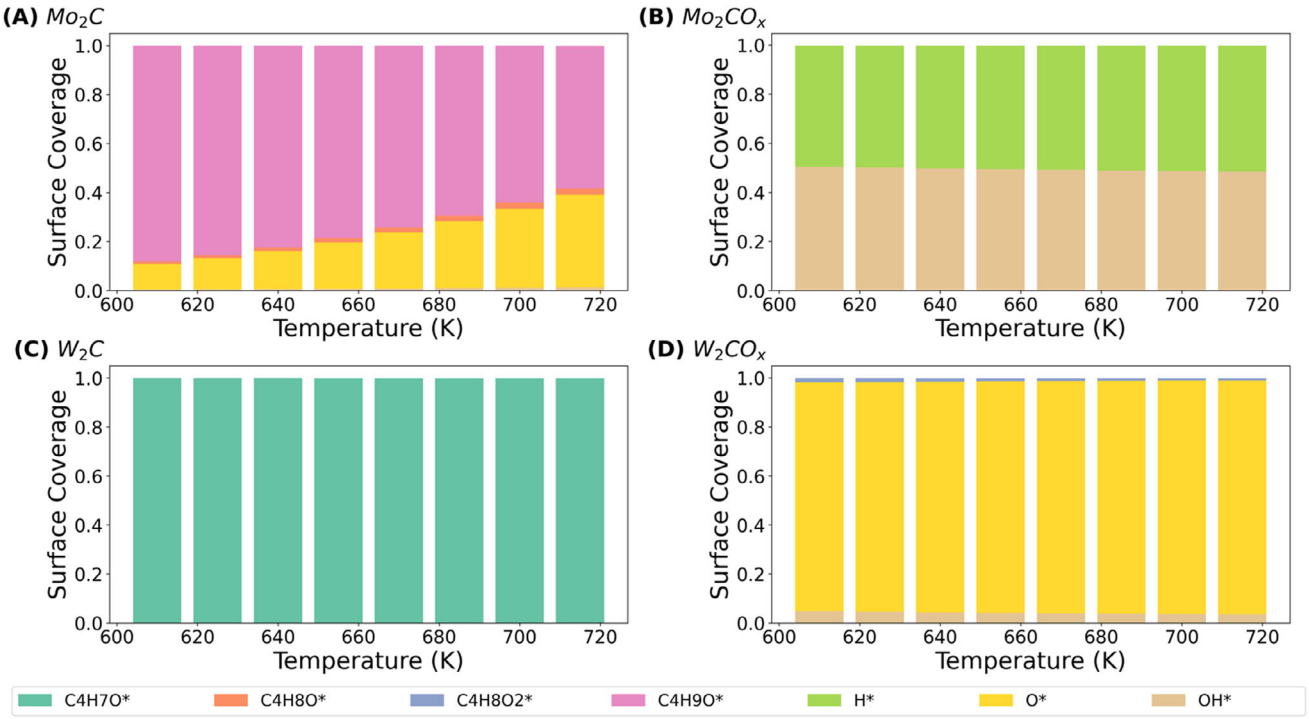

Figure 4. Steady state surface coverage as a function of temperature. Only the species with coverage > 0.005 are shown in the plots.

on the surface, hinting toward the possible formation of oxycarbide surface during the HDO reaction. However, that is not the case in W_2C (Figure 4C), where the reaction is very slow and the surface is dominated by the presence of $C_4H_7O^*$, a precursor for butanal (C_4H_8O) formation. On the other hand, in the case of Mo_2CO_x (Figure 4B), the surface is mostly dominated by OH* and H*, as water (H_2O^*) formation is kinetically and thermodynamically a difficult step ($E_a = 2.11$ eV, $\Delta E = 1.46$ eV). This shows that the Mo_2CO_x surface is robust and none of the intermediates and products are too stable on the surface, which makes the reaction faster. Also, the availability of excess H* species promotes the reaction, making it a more active catalyst than the rest. Whereas the surface of W_2CO_x (Figure 4D) is dominated by O* species, which shows that the surface is more robust than W_2C; but since the water formation ($OH^* + H^* \rightarrow H_2O^*$) is too difficult ($E_a = 2.00$ eV, $\Delta E = 2.00$ eV), the availability of excess H* promote the reactions.

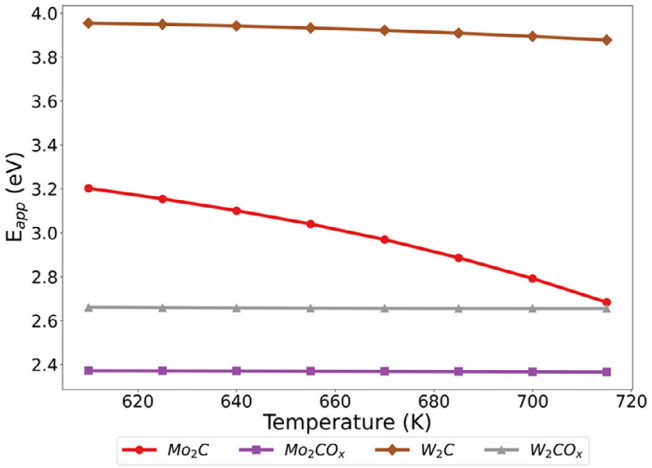

Figure 5. Apparent activation energy as a function of temperature.

2.7. Apparent Activation Energy (E_{app})

The apparent activation energies for the different catalysts are shown in Figure 5. It is evident that the activity of carbide catalysts increases as a function of temperature. While in the case of oxycarbide catalyst, the temperature does not influence the activity. Based on these results, we could conclude that Mo_2CO_x is the most active catalyst for butyric acid HDO at the reaction temperature of 623 K, with an apparent activation barrier of 2.40 eV, followed by W_2CO_x over which the apparent activation barrier is 2.70 eV. Both carbide catalysts are much less active compared to their oxycarbide counterparts. It is important to note that the higher HDO activity of Mo_2C catalyst compared to W_2C catalyst can be attributed to the ability of Mo_2C to partially oxidize (to form oxycarbide) their surface during the reaction, as revealed from the surface coverages (Figure 4A).

2.8. Degree of Rate Control (DRC) Analysis

DRC analysis reveals that, in all the cases, multiple elementary steps significantly contribute to the overall rate of the butyric acid HDO reaction (Figure 6). However, there is one elementary step, that is, butanol dissociation ($C_4H_9OH^* \rightarrow C_4H_9^* + OH^*$), which features in all the catalysts studied (**TS6** in Figures 2 and 3). These results indicated that butanol dissociation is one of the crucial steps in butyric acid HDO, irrespective of the

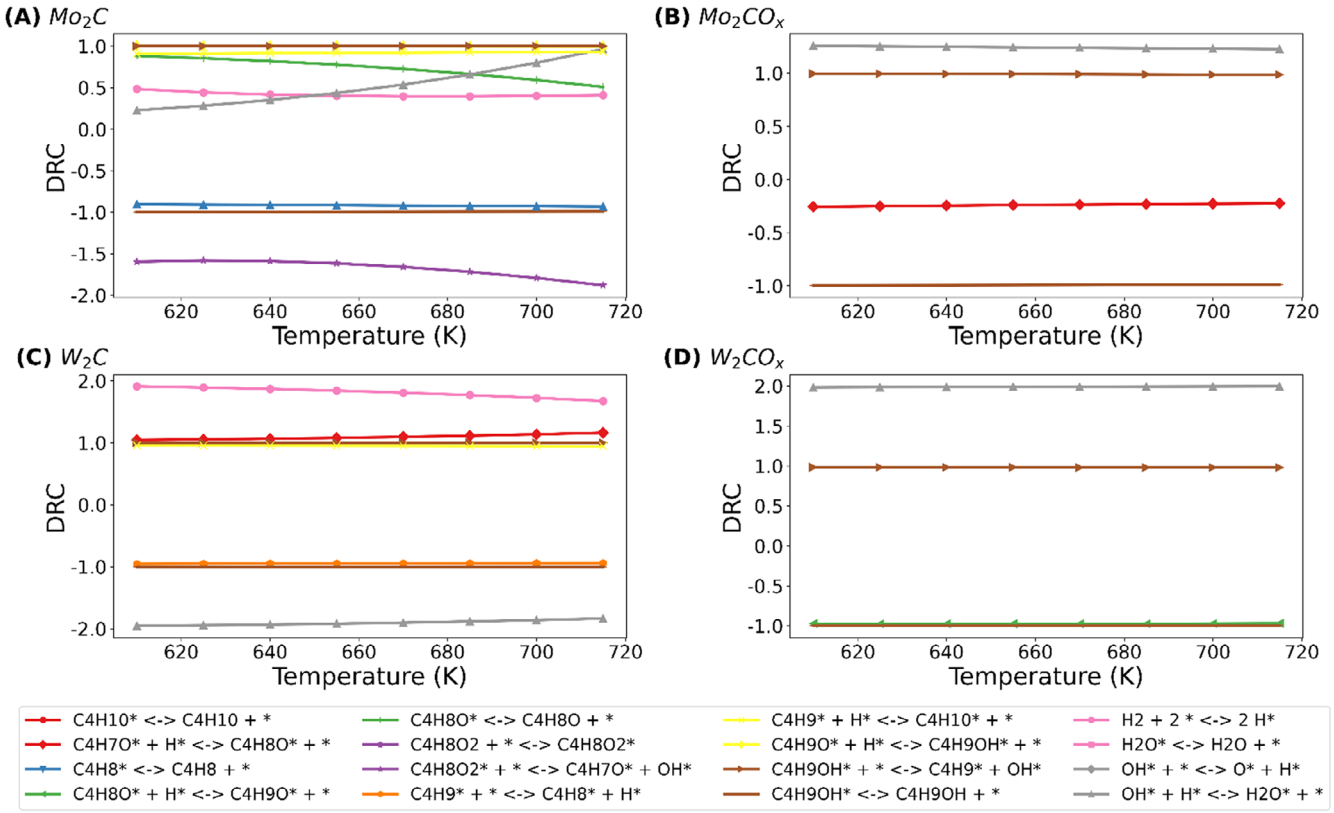

Figure 6. DRC coefficient as a function of temperature. Only the elementary steps with coefficients > 0.2 are shown in the plots.

catalyst, which can serve as a reaction descriptor for HDO activity examination. This is in line with the previous HDO studies, where C—OH activation was found to be the rate-determining step.[16,32,33] However, it is important to mention that the other rate-controlling elementary steps could also be considered for further optimization of these catalysts. For instance, the water formation is very difficult on TMOCs, and hence the OH* groups block the active sites; therefore, facilitating water formation on these surfaces could enhance the overall activity of the catalysts. Another interesting thing to notice is the difficulty of the hydrogenation steps in TMCs, possibly hinting toward scarcity of H* on the surface, as a result of easy water formation on TMCs compared to TMOCs. While water formation is easier on TMCs compared to TMOCs, the desorption of water molecules is still a challenge and possibly blocks the active sites. These insights could be used for optimization of these catalysts, by means of heteroatom doping, and vacancy formation. It is worth noting that here the desorption steps are not considered crucial as DFT-D3BJ is known to overestimate the long-range weak interactions,[34] resulting in larger DRC coefficients.

2.9. Selectivity Analysis

For all the calculated HDO reaction mechanisms, we checked their selectivity toward alkene (C_4H_8), and alkane (C_4H_{10}) products. From Figure 7, it is clear that carbides (Mo_2C, W_2C) are selective toward unsaturated hydrocarbons, that is, C_4H_8. In contrast, the oxycarbides (Mo_2CO_x, W_2CO_x) are selective toward saturated hydrocarbons, that is, C_4H_{10}. This selectivity of TMCs toward alkene products is in line with previous experimental and theoretical studies.[8,9,35] As highlighted in the DRC analysis, the availability of excess H* on the oxycarbide surfaces facilitates the hydrogenation reaction of C_4H_8 to C_4H_{10}. These observations are similar to the observations by Khoshooei et al. where they show that the activity of **α**-Mo_2C for reverse water gas shift increases as a function of H_2:CO_2 ratio, that is, in the presence of excess H*.[36]

3. Conclusions

In this work, we compared the reactivity of TMOCs (Mo_2CO_x, W_2CO_x) with TMCs (Mo_2C, W_2C) for the HDO reaction of *n*-butyric acid to *n*-butane. It is identified that Mo_2CO_x is the most active and selective catalyst for this HDO reaction, followed closely by W_2CO_x. The O* domains on the surface enhance the activity of these catalysts by easing the dissociation of the C-O bond and promoting the hydrogenation reactions due to excess H* on the surface, as compared to the pure TMCs. These insights imply the importance of controlling the carburization extent of the TMC catalysts to achieve high HDO activity and selectivity.

4. Computational Details

All DFT calculations have been performed using the Vienna Ab Initio Simulation Package (VASP).[37,38] The generalized

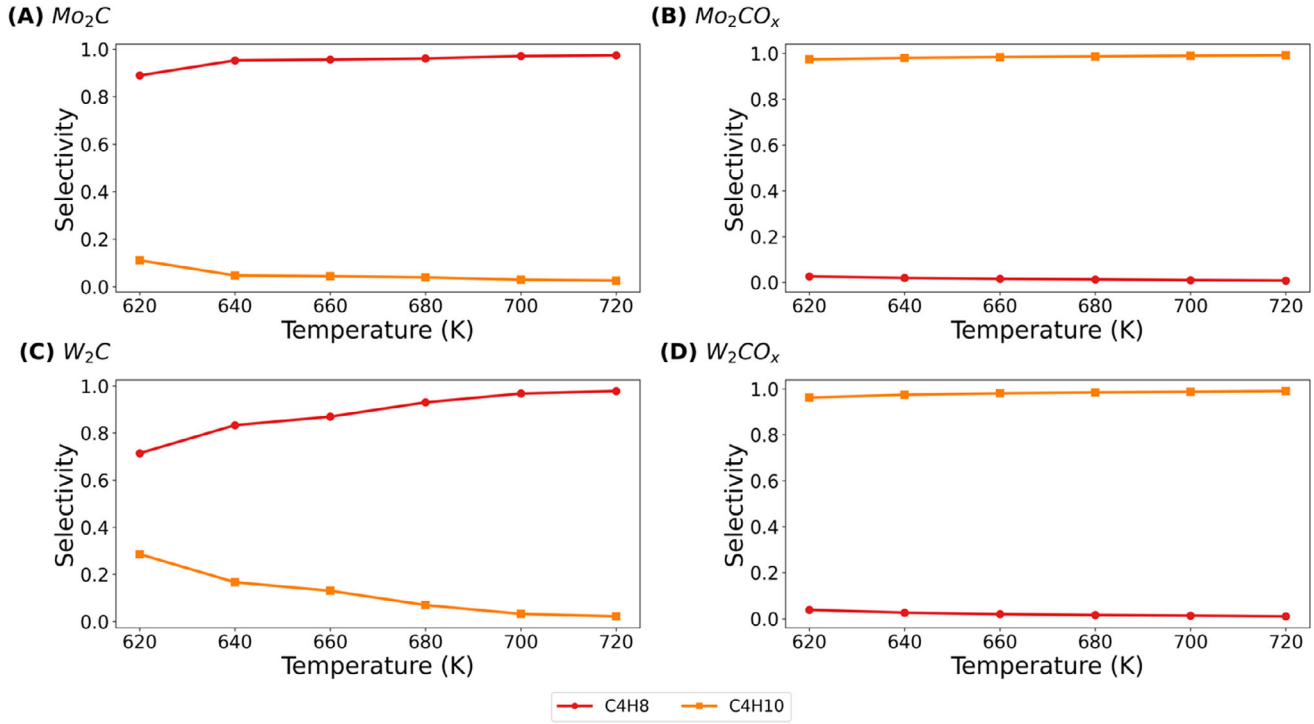

Figure 7. Selectivity toward alkane and alkene as a function of temperature. The y-axis is normalized for comparison.

gradient approximation (GGA) with the Perdew–Burke–Ernzerhof (PBE) exchange and correlation functional was used for the exchange-correlation energy.[39,40] The kinetic energy cut-off of the plane wave basis set was set to 500 eV. The convergence criterion for energy calculation and structure relaxation was set to a self-consistent field threshold of 10^{-5} eV, and a maximum force threshold of 0.05 eV/Å. Γ-centered k-meshes of the size of $6 \times 6 \times 6$ and $2 \times 2 \times 1$ were used for sampling the Brillouin zone in the case of bulk and slab models, respectively. Gaussian-type smearing with a width of 0.05 eV was applied for the electronic energy density of states. For identifying the transition states, the climbing-image nudged elastic band (CI-NEB) method was used, and frequency analysis was performed to confirm that there was only one imaginary frequency along the reaction coordinate.[41] For CI-NEB calculations, the maximum force threshold of 0.10 eV/Å was implemented. Dipole corrections were applied in the vacuum (z) direction. The van der Waals interactions were described by the DFT-D3BJ method developed by Grimme et al.[42,43] It is important to highlight that DFT-D3 is known to overestimate the binding energies of the reactants on the solid surface,[34] and therefore yields a larger desorption barrier for the reactant and product.

The bulk structures of orthorhombic Mo_2C (mp-1552) and orthorhombic W_2C (mp-2034) were obtained from the Materials Project website and were fully relaxed. The obtained lattice parameters for Mo_2C: a = 4.75 Å, b = 5.23 Å, c = 6.05 Å (from experiments: a = 4.74 Å, b = 5.21 Å, c = 6.03 Å), [27] and for W_2C: a = 4.75 Å, b = 5.24 Å, c = 6.09 Å (from experiments: a = 4.73 Å, b = 5.20 Å, c = 6.01 Å)[28] were in good agreement with the experimentally reported values. From the optimized bulk(s), we cleaved a stable (101) surface and built a unit cell with nine atomic layers thickness (three stoichiometric layers), as shown in Figure 1. Additionally, the carbon atoms in the top layer of TMCs were replaced by oxygen to create the TMOC surfaces, as in the study by Ammal et al.[21] For all the slab models, a vacuum distance of 15 Å was introduced in the z-direction to minimize interaction with the periodic images. After relaxing the atoms in the unit cell, we created a supercell of the size $2 \times 3 \times 1$, which was deemed to be a big enough surface for the HDO reaction. The bottom six atomic layers of the supercell were fixed to reduce the computational cost of the calculations and to mimic the bulk.

The adsorption energies (E_{ads}), reaction energies (ΔE), and activation barriers (E_a) were calculated as follows.

$$E_{ads} = E_{slab+reactant} - E_{slab} - E_{reactant} \quad (1)$$

$$\Delta E = E_{product} - E_{reactant} \quad (2)$$

$$E_a = E_{transition\ state} - E_{reactant} \quad (3)$$

Here, $E_{slab\ +\ reactant}$ is the total energy of the slab with a reactant adsorbed on it, E_{slab} is the total energy of the clean slab, $E_{reactant}$ and $E_{product}$ are the total energies of the reactant and product of each elementary reaction step, and $E_{transition\ state}$ is the total energy of the transition state (TS). The zero-point energies were corrected for all the elementary steps. The entropic contributions were considered for all the adsorption and desorption steps of gas-phase molecules.

Ab initio molecular dynamics (AIMD) simulations were performed using the CP2K-6.3 package.[44,45] An MD step length of

0.5 fs was used. The systems were allowed to evolve for 5 ps in the NVT canonical ensemble, equilibrated using a canonical sampling through velocity rescaling (CSVR) thermostat set at 623 K. The force field was computed using the PBE functional, and Grimme's DFT-D3BJ method was used to describe the vdW interactions.[42,43] Atoms were described using double-ζ molecularly optimized (MOLOPT) gaussian basis sets[46,47] and associated Goedecker–Teter–Hutter pseudopotential.[48]

The MKMCXX package was used for the microkinetic modelling (MKM) simulations.[49] MKM is a tool used to identify the critical intermediates and rate-determining elementary reactions. The chemo-kinetic network was modeled using a set of ordinary differential equations involving rate constants, surface coverages, and partial pressures of gas-phase species ($C_4H_8O_2$:H_2 as 1:3), $pH_2 = 30$ bar, and reaction temperature of 623 K. Time-integration of the differential equations was conducted using the linear multistep backward differential formula method with a relative and absolute tolerance of 10^{-8}.

The rate constant (k) of an elementary reaction step is given as:

$$\boldsymbol{k} = \frac{\boldsymbol{k_B T}}{\boldsymbol{h}} \frac{\boldsymbol{Q^{\neq}}}{\boldsymbol{Q}} \boldsymbol{e}^{(-\Delta E_a / k_B T)} \tag{4}$$

where $Q^{\neq}$ and Q are the partition functions of the activated complex and its corresponding initial state, respectively, and ΔE_a is the activation energy.

To identify the steps that control the butyric acid consumption rate and the product distribution, we performed the degree of rate control (DRC) analysis, as developed by Kozuch and Shaik,[50,51] and popularized by Campbell.[31]

The DRC coefficient is defined as:

$$\boldsymbol{X_{RC,i}} = \left(\frac{\partial \, \boldsymbol{lnr_i}}{\partial \, \boldsymbol{lnk_i}} \right)_{\boldsymbol{k_{j \neq i}, K_i}} \tag{5}$$

where $\boldsymbol{X_{RC,i}}$ is the degree of rate control coefficient, r_i the overall reaction rate, k_i the reaction rate constant for elementary reaction step i and K_i the equilibrium constant of elementary reaction step i.

While the sensitivity analysis was performed using the following equation:

$$\varepsilon_{\boldsymbol{i,c}} = \left(\frac{\partial \boldsymbol{\eta_c}}{\partial \, \boldsymbol{lnk_i}} \right)_{\boldsymbol{k_{j \neq i}, K_i}} \tag{6}$$

where $\varepsilon_{i,c}$ is the degree of selectivity coefficient (DSC) of compound c due to a change in elementary reaction step i and $\boldsymbol{\eta_c}$ is the selectivity of compound c.

Once the DRC coefficients are known, we can calculate the DSC using the following equation.

$$\varepsilon_{i,c} = \eta_c (X_{C,i} - X_{R,i}) \tag{7}$$

In other words, the DSC is the DRC using the rate of the compound you are interested in minus the DRC using the rate of the overall reaction (i.e., of a specific reactant), multiplied by the selectivity of the compound of interest. A positive DSC indicates that the selectivity of this compound will increase when the barrier of the corresponding elementary reaction step is lowered, whereas a negative value indicates that the selectivity decreases if the barrier is lowered.

Acknowledgements

The authors acknowledge the Dutch Organization for Scientific Research (NWO) for access to the Dutch national e-infrastructure (grants EINF-4916, EINF-7987, and NWO-2022.036).

Conflict of Interests

The authors declare no conflict of interest.

Data Availability Statement

The data that support the findings of this study are available from the corresponding author upon reasonable request.

Keywords: Biomass · Hydrodeoxygenation · Oxycarbide · Reaction mechanism · Transition metal carbides

[1] E. Furimsky, *Appl Catal A-Gen* **2000**, *199*, 147–190.
[2] C. O. Tuck; E. Pérez; I. T. Horváth; R. A. Sheldon; M. Poliakoff, *Science* **2012**, *337*, 695–699.
[3] R. W. Gosselink; S. A. W. Hollak; S. W. Chang; J. van Haveren; K. P. de Jong; J. H. Bitter; D. S. van Es, *ChemSusChem* **2013**, *6*, 1576–1594.
[4] S. Kim; E. E. Kwon; Y. T. Kim; S. Jung; H. J. Kim; G. W. Huber; J. Lee, *Green Chem.* **2019**, *21*, 3715–3743.
[5] M. Snåre, I. Kubičková, P. Mäki-Arvela, K. Eränen, D. Yu. Murzin, *Ind. Eng. Chem. Res.* **2006**, *45*, 5708–5715.
[6] S. T. Oyama, *Catal. Today* **1992**, *15*, 179–200.
[7] R. W. Gosselink, D. R. Stellwagen, J. H. Bitter, *Angew. Chem. Int. Ed. Engl.* **2013**, *52*, 5089–5092.
[8] S. A. W. Hollak, R. W. Gosselink, D. S. van Es, J. H. Bitter, *ACS Catal.* **2013**, *3*, 2837–2844.
[9] H. Ren, Y. Chen, Y. L. Huang, W. H. Deng, D. G. Vlachos, J. G. G. Chen, *Green Chem.* **2014**, *16* 761–769.
[10] D. R. Stellwagen, J. H. Bitter, *Green Chem.* **2015**, *17* 582–593.
[11] J. R. Kitchin, J. K. Nørskov, M. A. Barteau, J. G. Chen, *Catal. Today* **2005**, *105* 66–73.
[12] R. B. Levy, M. Boudart, *Science* **1973**, *181* 547–549.
[13] E. Iglesia, F. H. Ribeiro, M. Boudart, J. E. Baumgartner, *Catal. Today* **1992**, *15* 307–337.
[14] J. S. Choi, G. Bugli, G. Djéga-Mariadassou, *J. Catal.* **2000**, *193* 238–247.
[15] R. Meena, J. H. Bitter, H. Zuilhof, G. Li, *ACS Catal.* **2023**, *13* 13446–13455.
[16] M. Führer, T. van Haasterecht, J. H. Bitter, *Catal. Today* **2023**, *418*, 114108.
[17] H. Prats, M. Stamatakis, *J. Phys. Chem. Lett.* **2024**, *15* 3450–3460.
[18] J. A. Schaidle, J. Blackburn, C. A. Farberow, C. Nash, K. X. Steirer, J. Clark, D. J. Robichaud, D. A. Ruddy, *ACS Catal.* **2016**, *6* 1181–1197.
[19] C. J. Chen, A. Bhan, *ACS Catal.* **2017**, *7* 1113–1122.
[20] A. Kumar, S. Phadke, A. Bhan, *Catal. Sci. Technol.* **2018**, *8* 2938–2953.
[21] S. C. Ammal, A. Heyden, *ACS Catal.* **2023**, *13* 7499–7513.
[22] A. Kurlov, E. B. Deeva, P. M. Abdala, D. Lebedev, A. Tsoukalou, A. Comas-Vives, A. Fedorov, C. R. Müller, *Nat. Commun.* **2020**, 11.
[23] L. Óvári, J. Kiss, A. P. Farkas, F. Solymosi, *J. Phys. Chem. B* **2005**, *109* 4638–4645.
[24] X. R. Shi, S. G. Wang, J. G. Wang, *J Mol Catal a-Chem* **2016**, *417*, 53–63.
[25] X. Sun, J. Yu, H. Zada, Y. Han, L. Zhang, H. Chen, W. Yin, J. Sun, *Nat. Chem.* **2024**, *16*, 2044–2053.

[26] N. J. Luo, Z. F. Hou, C. S. Lin, G. L. Chai, *Cryst. Growth Des.* **2023**, *23* 5486–5497.
[27] K. Page, J. Li, R. Savinelli, H. N. Szumila, J. P. Zhang, J. K. Stalick, T. Proffen, S. L. Scott, R. Seshadri, *Sol. State Sci.* **2008**, *10* 1499–1510.
[28] E. Rudy, S. Windisch, *J. Am. Ceram. Soc.* **1967**, *50* 272.
[29] S. R. J. Likith, C. A. Farberow, S. Manna, A. Abdulslam, V. Stevanović, D. A. Ruddy, J. A. Schaidle, D. J. Robichaud, C. V. Ciobanu, *J. Phys. Chem. C* **2018**, *122* 1223–1233.
[30] H. Li, K. Reuter, *ACS Catal.* **2022**, *12* 10506–10513.
[31] C. T. Campbell, *ACS Catal.* **2017**, *7* 2770–2779.
[32] Y. Shi, Y. Yang, Y. W. Li, H. J. Jiao, *Catal. Sci. Technol.* **2016**, *6* 4923–4936.
[33] R. R. Oliveira, A. B. Rocha, *J. Mol. Model* **2019**, *25* 309.
[34] R. B. Araujo, G. L. S. Rodrigues, E. C. Dos Santos, L. G. M. Pettersson, *Nat. Commun.* **2022**, *13* 6853.
[35] H. Ren, W. Yu, M. Salciccioli, Y. Chen, Y. Huang, K. Xiong, D. G. Vlachos, J. G. Chen, *ChemSusChem* **2013**, *6* 798–801.
[36] M. Ahmadi Khoshooei, X. Wang, G. Vitale, F. Formalik, K. O. Kirlikovali, R. Q. Snurr, P. Pereira-Almao, O. K. Farha, *Science* **2024**, *384*, 540–546.
[37] G. Kresse, J. Furthmüller, *Comput. Mater. Sci.* **1996**, *6* 15–50.
[38] G. Kresse, J. Furthmüller, *Phys. Rev. B Condens. Matter.* **1996**, *54* 11169–11186.
[39] J. P. Perdew, A. Zunger, *Phys. Rev. B* **1981**, *23* 5048–5079.
[40] J. P. Perdew, K. Burke, M. Ernzerhof, *Phys. Rev. Lett.* **1996**, *77* 3865–3868.
[41] G. Henkelman, B. P. Uberuaga, H. Jónsson, *J. Chem. Phys.* **2000**, *113* 9901–9904.
[42] S. Grimme, J. Antony, S. Ehrlich, H. Krieg, *J. Chem. Phys.* **2010**, *132*, 154104.
[43] S. Grimme, S. Ehrlich, L. Goerigk, *J. Comput. Chem.* **2011**, *32* 1456–1465.
[44] J. Hutter, M. Iannuzzi, F. Schiffmann, J. VandeVondele, *Wires Comput. Mol. Sci.* **2014**, *4* 15–25.
[45] T. D. Kühne, M. Iannuzzi, M. Del Ben, V. V. Rybkin, P. Seewald, F. Stein, T. Laino, R. Z. Khaliullin, O. Schütt, F. Schiffmann, D. Golze, J. Wilhelm, S. Chulkov, M. H. Bani-Hashemian, V. Weber, U. Borštnik, M. Taillefumier, A. S. Jakobovits, A. Lazzaro, H. Pabst, T. Müller, R. Schade, M. Guidon, S. Andermatt, N. Holmberg, G. K. Schenter, A. Hehn, A. Bussy, F. Belleflamme, G. Tabacchi, A. Glöß, M. Lass, I. Bethune, C. J. Mundy, C. Plessl, M. Watkins, J. VandeVondele, M. Krack, J. Hutter, *J. Chem. Phys.* **2020**, *152 194103*.
[46] G. Lippert, J. Hutter, M. Parrinello, *Mol. Phys.* **1997**, *92* 477–488.
[47] J. VandeVondele, J. Hutter, *J. Chem. Phys.* **2007**, *127*, 114105.
[48] M. Krack, *Theor. Chem. Acc.* **2005**, *114*, 145–152.
[49] I. A. W. Filot, R. A. Van Santen, E. J. M. Hensen, *Angew. Chem. Int. Ed.* **2014**, *53* 12746–12750.
[50] S. Kozuch, S. Shaik, *J. Am. Chem. Soc.* **2006**, *128* 3355–3365.
[51] S. Kozuch, S. Shaik, *J. Phys. Chem. A* **2008**, *112* 6032–6041.

Manuscript received: April 10, 2025
Revised manuscript received: May 20, 2025
Accepted manuscript online: May 22, 2025
Version of record online: ■■, ■■